Comparing sintering and atomic layer deposition as methods to mechanically reinforce nanocolloidal crystals

Di Zhang, Yue Xu, and Gang Feng[a)]
Department of Mechanical Engineering, Villanova University, Villanova, Pennsylvania 19085, USA
Yun-Ru Huang[b)] and Daeyeon Lee
Department of Chemical and Biomolecular Engineering, University of Pennsylvania, Philadelphia, Pennsylvania 19104, USA

(Received 25 May 2015; accepted 27 October 2015)

Nanocolloidal crystals (NCCs) have promising applications in optical and photonic devices. However, it is critical to mechanically reinforce NCCs for device reliability, since as-synthesized NCCs are fragile due to weak interparticle bonding. Thermal sintering is currently the most common reinforcement technique; however, this method could induce serious cracking and is not suitable for temperature-sensitive materials. In this study, by characterizing silica NCCs reinforced through sintering and alumina atomic layer deposition (ALD), we find that the ALD treatment is much more effective for hardening, stiffening, and more importantly toughening NCCs. Thermally sintered NCCs are prone to indentation-induced cracking due to large residual tensile stress, significantly impairing the toughness. In contrast, the ALD treatment toughens NCCs by much over 300%. Our finding provides insights for reinforcing and toughening various nanoparticle-based and nanoporous materials.

I. INTRODUCTION

Nanocolloidal crystals (NCCs) have been intensively studied due to their promising applications, such as optical devices,[1] data storage,[2,3] waveguides,[4–6] and sensors.[7] However, their poor mechanical properties significantly hinder these applications.[8–12] Thermal sintering is the most common reinforcement technique for colloid assemblies.[13–20] Moreover, to synthesize inverse opals which are another type of emerging advanced optical materials, it is typical to use NCCs as infiltration templates which are usually pre-reinforced to maintain their integrity during the template-infiltration process,[11,21–32] for example, SiO_2 NCC templates are commonly sintered at temperatures above 800 °C,[21–26,28,30–32] and polystyrene NCC templates are commonly sintered at 80–85 °C.[11,29]

The initial stage of sintering-induced reinforcement of colloid assemblies involves the formation of interparticle neck through various mechanisms, such as surface diffusion, volume diffusion, evaporation-condensation, and plastic/viscous flow.[20,33–37] The dynamics of neck growth depends strongly on sintering temperature T_s, particle size, and the associated neck-formation mechanism(s).[20,33–37] For example, Poppe quantitatively studied the effects of sintering temperate and duration on neck growth for monodisperse SiO_2 micro-colloids (MCs).[33] Poppe found that[33] the SiO_2 MC assembly has a melting temperature of ~1250 °C, and that significant sintering-induced neck formation occurs at $T_s \gtrsim 1000$ °C. Also, the dominant mechanism of neck transitions from surface diffusion to viscous flow at ~1150 °C. It was also found that the neck growth depends strongly on the sintering temperature T_s but weakly on the sintering duration t_s (neck radius $\propto \sim t_s^{1/6}$ at a T_s).[33]

The effects of sintering on the structure and optical properties of NCCs have also been extensively studied.[14–17,19] Many of these studies have shown that that sintering can induce crack formation and film delamination,[16,17,24] jeopardizing the optical properties of NCCs.[16,17,24] Moreover, high temperature sintering may preclude the use of NCCs on polymer substrates, commonly used for flexible electronics. Despite these prior reports, surprisingly little is known about the effects of sintering on the mechanical properties of NCCs.

Material infiltration has been considered as another approach for reinforcing NCCs,[38–41] although such an approach is typically used to fabricate inverse opals from NCCs.[11,27–29,42] Based on our previous studies,[38,39] the associated reinforcement mechanism is interparticle bonding (IPB) induced by materials deposition at interparticle junctions.[38–41] The mechanism is also earlier observed by Gallego-Gómez et al.,[10,40] and they found that, after establishing interparticle bonds in silica NCCs by replicating

Contributing Editor: Yang-T. Cheng
[a)]Address all correspondence to this author.
e-mail: gang.feng@villanova.edu
[b)]Author's present affiliation is: Department of Chemical Engineering, Carnegie Mellon University, Pittsburgh, Pennsylvania 15213, USA.
DOI: 10.1557/jmr.2015.347

 © Materials Research Society 2015

https://doi.org/10.1557/jmr.2015.347 Published online by Cambridge University Press

the interparticle capillary bridges with chemical vapor deposition (CVD)-silica, each NCC behaves as a monolithic nanoframe with much less creep compared to the as-assembled counterparts. CVD[32,41,43–45] and atomic layer deposition (ALD)[8,9,38,39,46,47] have been used for infiltration-based mechanical reinforcement. Compared to conventional CVD, ALD process involves self-limiting surface reactions, enabling precise control of deposition and provides superior film conformity and uniformity.[48–52] It should be mentioned that, Blanco et al.[53] and Gallego-Gómez et al.[40,54] recently reported a "one-pulse CVD" process by eliminating any water cycles; thus, the precursor reacts only with water pre-adsorbed in the structure, which is also self-limiting by nature and produces precisely-controlled deposition.

In our previous studies, ALD treatment has been shown to significantly harden and stiffen disordered nanoparticle assemblies[8,9] as well as NCCs.[38,39] For example, after Al_2O_3 ALD treatment, the SiO_2 NCCs can be drastically stiffened by a factor of 30 and hardened by a factor of 150,[39] and the unstable deformation of NCCs can be also largely suppressed.[38] It was found that, the ALD-treatment allows the precise tuning of the IPB by depositing a reinforcing layer around all of the nanocolloids (NCs) in NCCs.[39] By increasing the ALD thickness, the deformation mechanism of NCCs transitions from granular to bonded granular and, finally, to particle-reinforced composite behavior.[39]

Thus, both sintering and infiltration treatments can be used to reinforce NCCs, and tuning IPB is the major reinforcing mechanism for both approaches. However, as aforementioned, little is known about the effects of sintering on the mechanical properties of NCCs. This article provides the first quantitative comparison on the reinforcement due to sintering and ALD treatments. The effects of two approaches on the fracture behavior of NCCs are also discussed in first time.

In this study, sintering and Al_2O_3-ALD are used to mechanically reinforce NCCs composed of monodisperse 254 and 289 nm SiO_2 NCs. The reinforcement effects of these two techniques are systematically studied and compared using nanoindentation. We find that the ALD treatment is more effective in stiffening, hardening, and toughening NCCs without causing significant morphology change.

II. EXPERIMENTAL

Monodisperse 254 ± 19 and 289 ± 13 nm SiO_2 NCs were synthesized using the Stöber method.[55] Subsequently, NCCs (>10 μm thick) were prepared using the convective self-assembly method[56–58] on Si(001) substrate at 27 °C and relative humidity of 67%. In the paper, unless otherwise specified the NCCs refer to the 254 nm NCCs. The reflectance spectra of as-assembled NCCs were characterized using a Filmetrics F40-UVX system (Filmetrics, Inc., San Diego, California) with 250 μm aperture and 10× objective.

The 254 nm NCCs were sintered at 850, 950, 1000, and 1100 °C for 1 h, respectively, and a 3 h-850 °C sintering was also conducted. For each sintering process, the temperature ramp rate was 5 °C/min, and the furnace was powered off immediately after sintering; the samples were not taken out until the furnace was naturally cooled to room temperature.

Al_2O_3 ALD of up to 144 cycles was performed at 150 °C using a Savannah 200 from Cambridge Nano-Tech, Inc. (Waltham, Massachusetts). For simplicity, throughout this paper, "#ALD" represents the number of ALD cycles; for example, "15ALD 254 nm NCC" represents a 15-cycle-Al_2O_3-ALD-treated NCC composed of 254 nm SiO_2 NCs. Based on our previous studies on the similar systems,[38,39] the ALD growth rate is found to be ~0.07 nm/cycle.

The topography was characterized using a Hitachi S-4800 scanning electron microscope (SEM; Hitachi Ltd., Tokyo, Japan). The mechanical properties were characterized using a Nano Indenter™ G200 from Keysight™ Technologies, Inc. (Santa Rosa, California) with continuous stiffness measurement (CSM) capability. A diamond cube-corner tip was used with its area function being calibrated in 20–1800 nm. Prior to indentation, the indenter was stabilized with the thermal drift rate <0.05 nm/s. At least eight CSM-mode 1 μm and 2 μm-deep indentations were conducted on each sample using a constant loading-rate-to-load-ratio at 0.05 s^{-1}. The hardness H and modulus E were calculated using the Oliver–Pharr method[59] by averaging the corresponding CSM results in 800–1000 nm. The Hay method[60] was then used to correct the substrate effect on modulus E. The substrate effect on hardness H is generally negligible,[61] because the indentation depth (≤2 μm) is less than 20% of the NCC film thicknesses.

III. RESULTS AND DISCUSSIONS

SiO_2 NCCs composed of monodisperse NCs are normally in face-center-cubic (FCC) structure.[38,39] The NCCs of high quality would be ideal material systems to systematically and quantitatively study the effects of ALD and sintering treatments due to the ordered structure and associated high symmetry.

Figures 1(a) and 1(b) show the top-view and cross-sectional SEM images of 254 nm NCCs, indicating good particle monodispersity and highly ordered structure. The SEM images of 289 nm NCCs (see Fig. 1 of Ref. 39 for the same NCCs) also indicate high crystal quality. Moreover, the quality of each NCC can be evaluated by the maximum intensity I_{max} of the Bragg reflectance peak in reflectance spectrum, and $I_{max} \geq 80\%$ normally

https://doi.org/10.1557/jmr.2015.347 Published online by Cambridge University Press

indicates very high crystal quality.[44,62] Figure 1(c) shows I_{max} = 87% and I_{max} = 80% for 254 and 289 nm NCCs, respectively, again indicating very high crystal quality.[40,63] Here, the position of (111) and Bragg peaks of a FCC crystal at the normal incidence condition can be calculated by[40,63]

$$\lambda = 2d_{111}n_{\text{eff}} = 2\sqrt{\frac{2}{3}}d\sqrt{n_{\text{p}}^2\phi + n_{\text{m}}^2(1-\phi)} \quad , \qquad (1)$$

where d is particle diameter; $d_{111} = d\sqrt{(2/3)}$ is the (111) plane spacing; n_{eff} is the effective refractive index; ϕ is particle volume fraction (~0.74 for FCC packing); n_{p} and n_{m} are the refractive indices of the SiO_2 nanoparticles (~1.425)[64,65] and the air medium (~1.0), respectively. Thus, based on Eq. (1), the theoretical peak positions for 254 ± 19 and 289 ± 13 nm NCCs would be 551 ± 41 and 627 ± 28 nm, respectively, matching nicely with the experimental results (569.2 and 617.3 nm) shown in Fig. 1(c).

The as-assembled 254 nm NCCs have hardness H of 0.05 ± 0.01 GPa and modulus E of 1.6 ± 0.2 GPa. Figure 1(d) shows the H and E of untreated and sintered 254 nm NCCs, indicating that 850 °C is the minimum

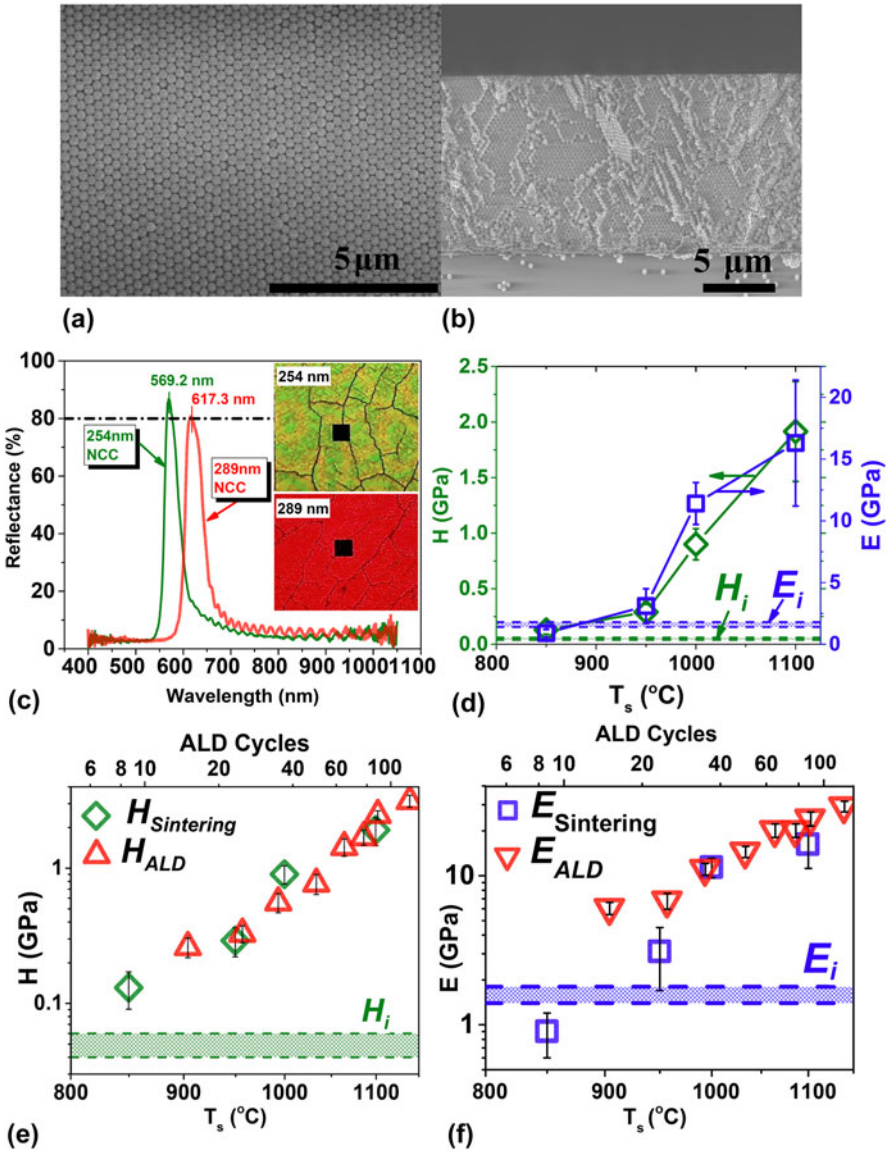


FIG. 1. (a) Top-view and (b) cross-sectional SEM images of a 254 nm NCC. (c) The reflectance spectra of 254 and 289 nm NCCs. The inserted images are the testing spots for the reflectance spectra in 254 and 289 nm NCCs. The spot size is 25 × 25 μm. (d) Hardness H and modulus E of 254 nm NCCs versus sintering temperature T_s. (e) H and (f) E of 254 nm NCCs versus T_s (bottom coordinate) and ALD cycles (top coordinate) in log–log plot. The corresponding values of untreated 254 nm NCC are shown as horizontal dash lines, and each error bar is shown as a shaded region.

https://doi.org/10.1557/jmr.2015.347 Published online by Cambridge University Press

temperature required to achieve appreciable mechanical reinforcement after 1-h-sintering, consistent with the literature results.[11,13–18,21–29,42] Sintering duration is also important, e.g., the 3-h-850 °C sintered NCC has $H = 0.26 \pm 0.12$ GPa and $E = 2.4 \pm 1.15$ GPa, almost equivalent to those ($H = 0.29 \pm 0.07$ GPa, $E = 3.1 \pm 1.4$ GPa) with 1-h-950 °C treatment, and significantly larger than those ($H = 0.13 \pm 0.04$ GPa, $E = 0.9 \pm 0.3$ GPa) with 1-h-850 °C treatment.

To directly compare the effects of ALD and sintering, Fig. 1(e) is plotted by empirically power-law-correlating T_s and ALD-cycle n that result in the same hardness, which gives $T_s = 670n^{1/9}$. The *same* correlation ($T_s = 670n^{1/9}$) is applied to plot the moduli E of sintered and ALD-treated NCCs as a function of temperature and n, respectively [Fig. 1(f)]. Figures 1(e) and 1(f) indicate that both H and E exponentially increase with increasing T_s and n. For example, for $T_s = 1100$ °C, H and E increase 3700 and 900%, respectively, compared to those of as-assembled NCCs. At 120ALD, H and E increase 6400 and 1830%, respectively.

The hardening and stiffening of NCCs are due to the development of IPB.[38–40] As shown in Figs. 2(a) and 2(e), the indentation on 850 °C-sintering and 15ALD 254 nm NCCs result in a rigid-granule-like behavior without permanent deformation of *individual* NCs, resembling the indents on as-assembled NCC [see Fig. S1 (a) in Supplementary Material].[38–40] The granular behavior indicates weak IPB. Figure 2 also shows that, by increasing T_s or ALD cycle number, the permanent deformation and/or fracture of *individual* NCs are increasingly pronounced, especially when $T_s \geq 1000$ °C and ALD-cycle ≥ 50, indicating substantially stronger IPB.

Figure 2 interestingly shows that, the indentation of ALD-treated and sintered NCCs with the same hardness results in similar morphology, suggesting that IPB is increased in both cases. Thus, by increasing IPB through either sintering or ALD, the NCC deformation mechanism transitions from the granular behavior with weak IPB [see Figs. 2(a) and 2(e)] to granular behavior with strong IPB [see Figs. 2(c) and 2(g)], and then to monolith-like behavior [see Figs. 2(d) and 2(h)]. This mechanism transition in sintered and ALD-treated NCCs agrees well with our previous study on ALD-treated NCCs,[39] which is also consistent with the observation of Gallego-Gómez et al.[10,40] that the NCC's behavior would transit from granular to nongranular/monolithic after CVD infiltration into the NCC structure.

The sintering-induced IPB can be qualitatively confirmed by the formation of freestanding NC-chains inside a sintering-induced crack as shown in Fig. 3. No such NC-chain is observed in the as-assembled NCCs [see Fig. S1(b) in Supplementary Material]. It is interesting that the interparticle necking becomes observable only at $T_s \gtrsim 1000$ °C, corresponding to strong IPB as implied by Figs. 2(c) and 2(d), which is consistent with Poppe's observation for 1.556 μm SiO_2 MCs.[33] We believe that, for T_s in the range of 850–1000 °C, the interparticle necking is also formed, as implied by the formation of freestanding NC-chains [see Figs. 3(a) and 3(b)] and also the hardening and stiffening of the NCCs [see Fig. 1(d)], but the size of the necking is below the resolution/image-noise limit of SEM.

It should be also noted that, as shown in Fig. 1(f), for NCCs that have comparable hardnesses, ALD treatment induces higher modulus than sintering; that is, ALD is more effective in stiffening than sintering, which may be

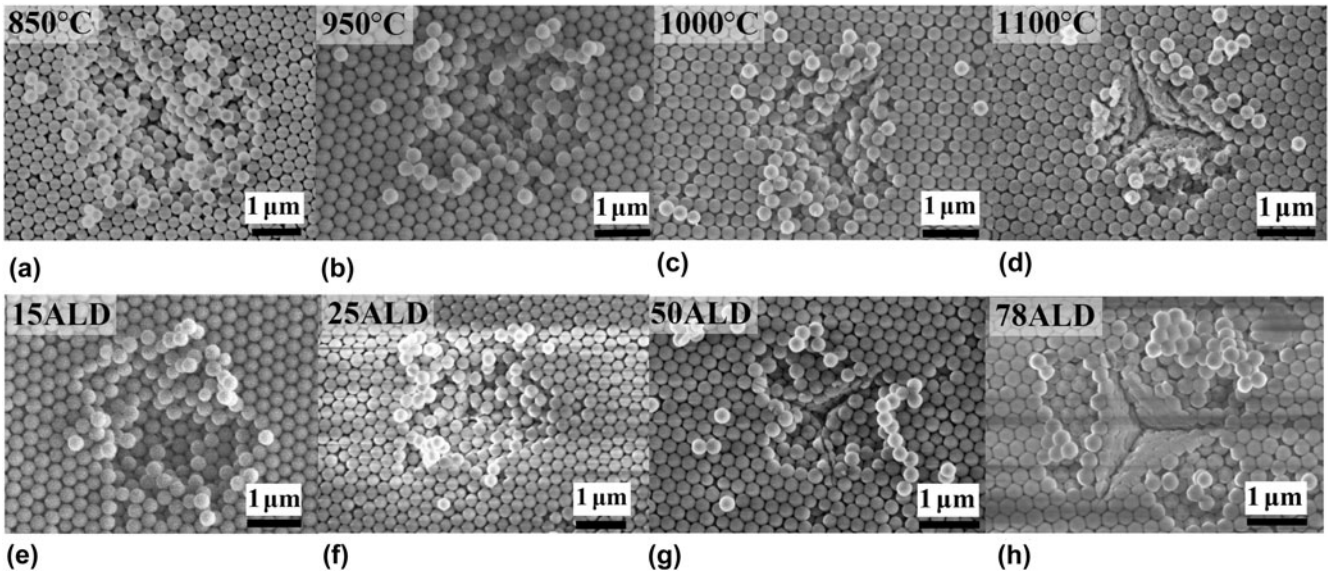


FIG. 2. SEM images of ~1 μm indents on (a)–(d) sintered and (e)–(h) ALD-treated 254 nm NCCs. The sintering temperature and #ALD are labeled. Here, each vertical pair [e.g., (a) and (e)] correspond roughly to the same hardness.

https://doi.org/10.1557/jmr.2015.347 Published online by Cambridge University Press

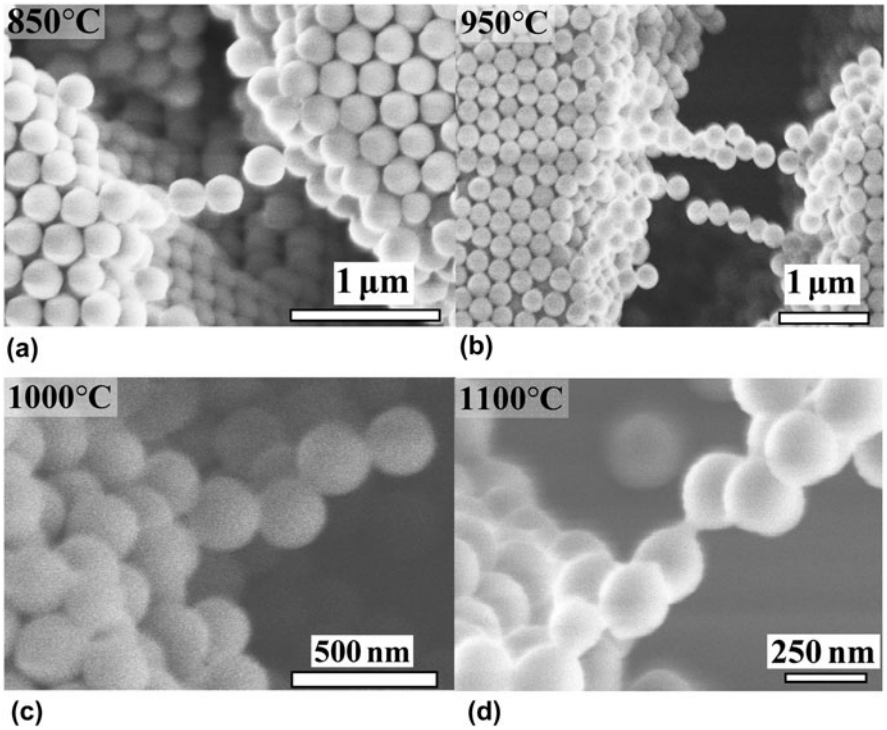


FIG. 3. SEM images of 1-h-sintering-induced cracking gaps, showing freestanding NC chains. The sintering temperatures are labeled.

qualitatively understood by the fact that Al_2O_3 ALD introduces a stiffer second phase (Al_2O_3) into SiO_2 NCCs, i.e., an additional stiffening effect compared to sintering. To quantitatively investigate this additional stiffening effect on NCCs due to the second phase introduced by ALD,[8] using various ALD materials would be needed,[8] which will be left for a future work.

In the following, we want to discuss the effects of sintering and ALD on suppressing NCCs' unstable deformation. As-assembled NCCs show unstable deformation, manifested as pop-ins upon nanoindentation.[10,38,40] In our previous study,[38] we found that the ALD-treatment significantly suppresses the unstable deformation. Here, we will show that sintering introduces a very similar effect.

Figures 4(a) and 4(b) show the typical indentation load–displacement (P–h) curves for the as-assembled as well as the sintered and ALD-treated NCCs of 3 conditions as labeled, indicating multiple pop-ins. A pop-in is a sudden increase of displacement without the associated load increase.[62,66,67] Gallego-Gómez et al.[10] also observed pop-ins upon indenting 335 nm SiO_2 NCCs. We have discussed the mechanism transition of pop-ins in untreated NCCs in a separated paper.[38] It was found that, by deepening indentation, the unstable deformation mode of untreated NCCs transitions from NC dislodging to shear band formation.[38]

Figures 4(c) and 4(e) plot the pop-in initiation/start displacement h_s and pop-in-termination/end displacement h_e as a function of the load of the 1st *pop-in* P_{1st} for ALD-treated and sintered samples, respectively. Figures 4(c) and 4(e) show that, for each treatment condition, h_s, h_e and Δh ($=h_e - h_s$) of the 1st *pop-in* are roughly proportional to P_{1st}. Moreover, Figs. 4(c) and 4(e) show that h_s, h_e and Δh at the same P_{1st} decreases significantly by increasing ALD cycle or sintering temperature, indicating that both sintering and ALD treatments suppress the unstable deformation of NCCs.[38] The same trend is observed for all treatment conditions considered in this study [see Figs. S2(a) and S2(b) in Supplementary Material]. It should be mentioned that, because the 1 and 2 μm indentation depths are relatively shallow, according to our previous work,[38] the pop-ins would fall into the particle-dislodging regime, which is consistent with the indentation morphology shown in Fig. 2.

The slope η_s ($=dh_s/dP_{1st}$) of h_s of each sample is also labeled in Figs. 4(c) and 4(e). It is interesting to see that, for reinforced NCCs with similar hardness, the values of η_s are very close to each other by comparing the plots of each sintering-ALD pair (e.g., 1.22–1.32 for 25ALD-950 °C, or 0.48–0.56 for 50ALD-1000 °C), implying that sintering and ALD treatments experience similar reinforcement mechanism. This similarity is consistent with the conclusion based on the indent morphology similarity (see Fig. 2). Moreover, as labeled in Figs. 4(c) and 4(e), the slopes η_e ($=dh_e/dP_{1st}$) of h_e have the same trend (e.g., 1.64–1.7 for 25ALD-950 °C, or 0.56–0.64 for 50ALD-1000 °C) by comparing the plots of each sintering-ALD pair.

https://doi.org/10.1557/jmr.2015.347 Published online by Cambridge University Press

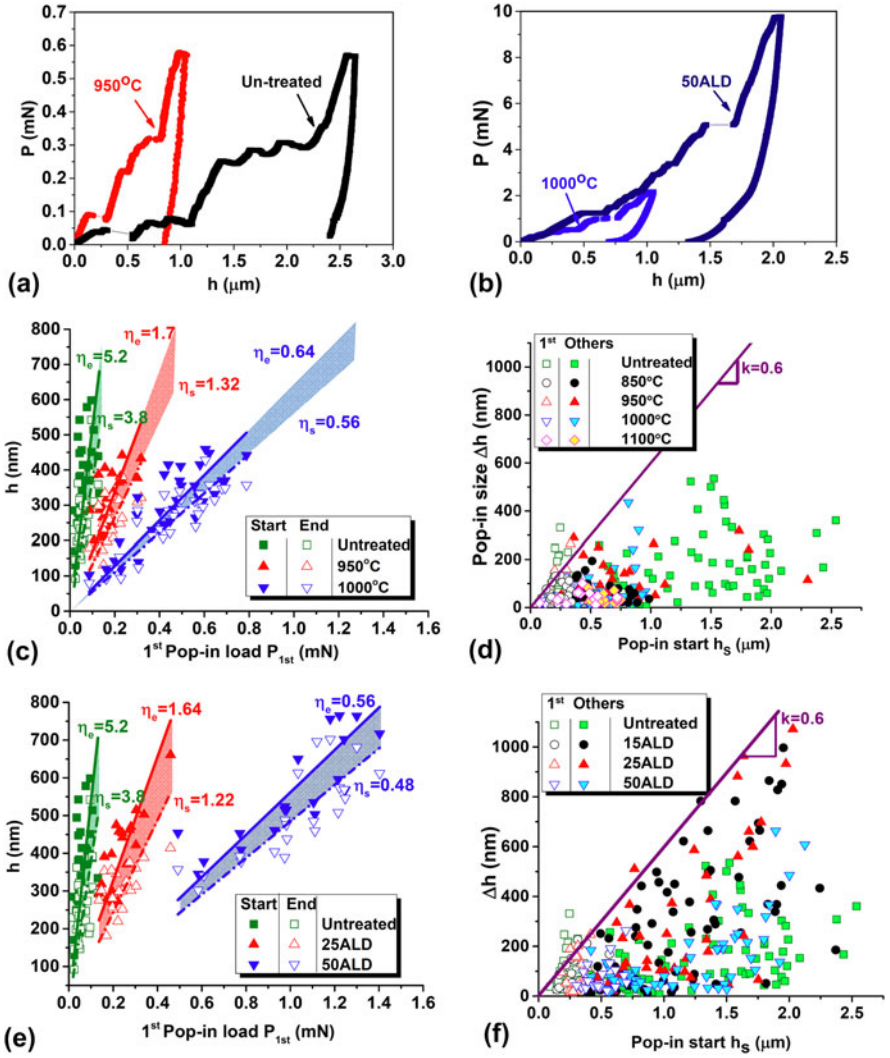


FIG. 4. Load P versus displacement h for (a) untreated and 950 °C-sintered and (b) 50ALD and 1000 °C-sintered 254 nm NCCs. The pop-in-start displacement h_s and pop-in-end displacement h_e of 1st pop-in versus the 1st pop in load P_{1st} for (c) sintered and (e) ALD-treated 254 nm NCCs, where the slopes η_s ($=dh_s/dP_{1st}$) and η_e ($=dh_e/dP_{1st}$) are also labeled for each sample. Pop-in size Δh ($=dh_e - dh_s$) versus h_s for (d) sintered and (f) ALD-treated 254 nm NCCs. Here, for easy comparison, we choose the same symbols for each sintering condition in (d) and the corresponding #ALD in (f) with the similar hardness.

Figures 4(d) and 4(f) show the plots of Δh versus h_s for *all* recorded pop-ins for sintered and ALD-treated samples, respectively, showing a roughly common upper Δh envelope of $\Delta h_{max} \approx 0.6h_s$ for $T_s \leq \sim 1000$ °C or ALD cycle $\leq \sim 25$. Moreover, Fig. 4(f) shows that the Δh envelop drops well below $0.6h_s$ for 50ALD, and Fig. 4(d) shows only a very few small (<100 nm) pop-ins for $T_s =$ 1100 °C. In fact, the pop-in phenomenon completely disappears at 78ALD for ALD-treated samples. Consequently, $T_s > 1100$ °C or ALD cycle > 50 can significantly suppress or completely eliminate the unstable deformation of NCCs. The trend of Δh envelope indicates again that the deformation mechanism is undergoing the following transition: from granular behavior with weak IPB ($T_s < 1000$ °C or ALD cycle < 50) to granular behavior with strong IPB ($T_s \approx 1000$ °C or ALD cycle ≈ 50), and then to monolith-like behavior ($T_s \geq \sim 1100$ °C or ALD cycle $\geq \sim 78$). The pop-in behavior of sintered and ALD-treated 254 nm NCCs matches nicely with the results of our previous study on ALD-treated 289 nm NCCs.[38]

In summary, both sintering and ALD treatments can locally harden and stiffen NCCs and at the same time suppress the unstable deformations of NCCs. However, in the following, we discuss a serious issue associated to sintering—that is, cracking which significantly degrades the film-integrity and functionality.[14–17,19] On the contrary, we find that the ALD-treatment can harden, stiffen, and also simultaneously toughen the NCC without inducing further cracks.

Figure 5(a) shows that cracks may form in as-assembled NCCs due to capillary stress during solvent evaporation in

https://doi.org/10.1557/jmr.2015.347 Published online by Cambridge University Press

the self-assembly process,[68–70] which however has minimal impact on the optical properties of NCCs[16,17,24] likely due to the small gaps present in these cracks [see Fig. 5(a)]. As aforementioned, sintering has been used to reinforce inorganic NCCs.[11,13–18,21–29,42] However, Figs. 5(b) and 5(d) clearly show that, due to the densification-induced residual biaxial-tensile stress,[71] sintering significantly widens the primary cracks formed during self-assembling and at the same time creates and widens secondary cracks. The crack widening effect becomes significant [see Fig. 5(b)] even at 850 °C (i.e., the minimum T_s for effective sintering), and the effect becomes increasingly severe upon further increasing T_s. For example, for T_s = 1000 °C, some crack gaps can be wider than 10 μm, which is equivalent to the thickness of the NCC. It is well known that the sintering-induced cracks can seriously jeopardize the optical properties of NCCs.[16,17,24]

Besides creating and widening cracks, sintering also significantly lowers NCCs' resistance to external penetration due to residual biaxial tensile stress.[24,72] For example, for $T_s > 850$ °C, any indentation larger than 2 μm in depth induces unstable and severe cracks propagation extending all the way to the NCC domain boundary and/or film delamination [see Fig. 5(d)].

In stark contrary, ALD reinforces NCCs because of the second phase material infiltration, which does not induce residual tensile stress. Consequently, the ALD-treatment (even at 144ALD) does not widen the primary cracks formed during self-assembly as shown in Fig. 5(e).

To quantify the toughening effect of ALD treatment, the fracture toughness K_c is determined based on indentation-induced half-penny cracking, which can be calculated by[73,74]

$$K_c = \alpha \left(\frac{E}{H}\right)^{\frac{1}{2}} \left(\frac{P_{max}}{c^{3/2}}\right) \quad , \qquad (2)$$

where P_{max} is the peak indentation load, E is Young's modulus, H is the hardness, and c is the surface-trace length of the half penny crack (see Fig. S4 for indentation-induced cracks for a 144ALD treated 289 nm NCC) measured from the indent center.[75–78] α is an empirical constant depending on the indenter geometry and is 0.032 for a cube-corner indenter.[75–78]

None of the 2 μm indentations on as-assembled 254 nm NCCs show indentation-induced cracks, so we could not calculate K_c. On the other hand, it is surprising to see that, at the nominally same 2 μm indentation, the as-assembled 289 nm NCCs show bimodal indentation fracture behavior: ~40% indentations show no cracks [see Fig. S3(b)], while others (~60% indentations) introduce very long cracks [see Fig. S3(a)] which are normally not terminated until intersecting with the intrinsic cracks (i.e., domain boundaries).

This bimodal indentation fracture behavior may be resulted from the different residual capillary (RC) stress in different film domains [see Figs. S3(a) and 5(a)]. Here, intrinsic cracks developed during drying process relax the capillary stress and define the domains. However, RC stress may exist and be different from domain to domain. Particularly, in some domains, the RC stress may be still large enough to provide high driving force for cracking, so these domains are prone to initiating and expanding cracks upon indentation [see Fig. S3(a)].[79,80] On the other hand, in some other domains, the RC stress may be close to zero, and Fig. S3(b) implies that the indentation-induced stress alone is not enough to initiate any cracks.

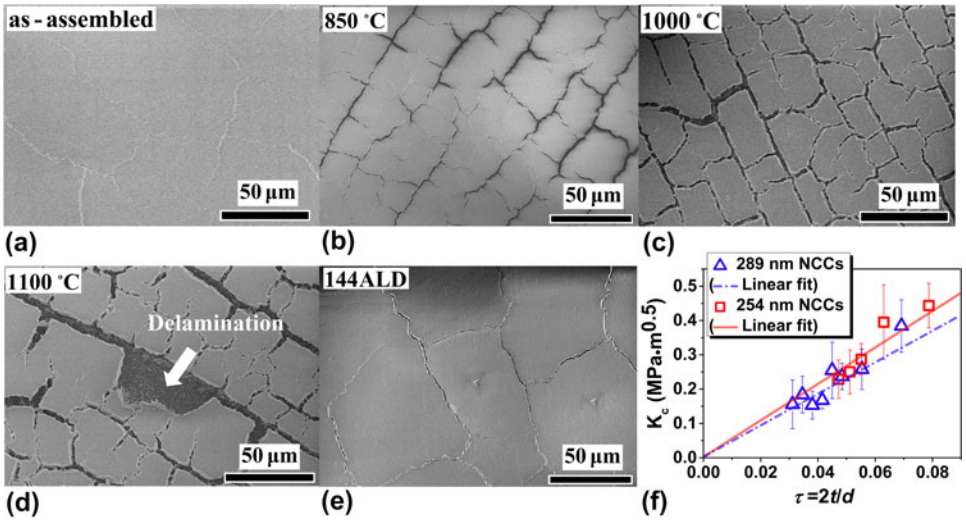


FIG. 5. (a)–(e) SEM images of as-assembled, sintered and ALD-treated NCCs as labeled. Here, in (d), a 2-μm-indentation-induced film delamination can be seen in the middle (one piece of film together with the indent on it was delaminated and missing as labeled). The scale bar is 50 μm in (a–e). (f) Fracture toughness K_c versus the normalized ALD thickness $\tau = t/(d/2)$ for ALD-treated 289 and 254 nm NCCs based on the WDWC indentation-induced cracks, where t is the ALD thickness (=#ALD × 0.07 nm/cycle), and $d/2$ is the particle radius.

https://doi.org/10.1557/jmr.2015.347 Published online by Cambridge University Press

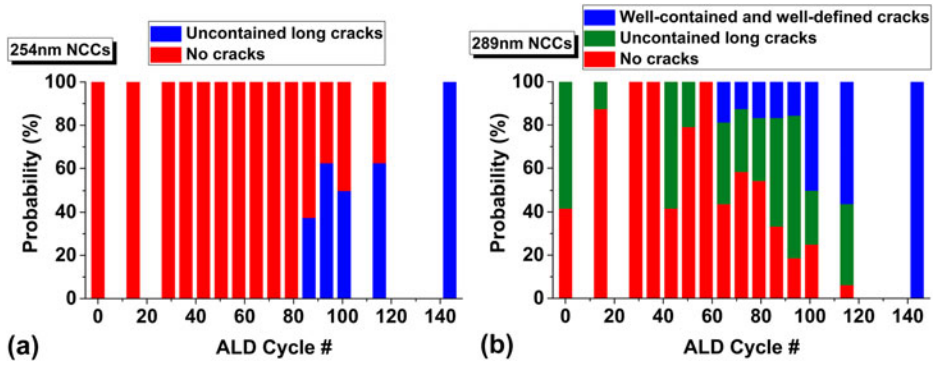


FIG. 6. The probabilities of three indentation-induced cracking modes for as-assembled and ALD-treated NCCs composed of (a) 254 nm NCs and (b) 289 nm NCs: (i) no cracking, (ii) uncontained long cracking, and (iii) WDWC indentation-induced cracking.

Thus, the driving force for the long cracks [see Fig. S3(a)] may involve both the indentation and RC stresses,[79,80] so we could not use Eq. (2) which is valid for cracking due to indentation stress alone.

Therefore, we cannot conclusively determine K_c for the as-assembled NCCs. Although increasing P_{max} would increase the crack length and possibility of indentation cracking,[75,76] the substrate's influence to the indentation stress field for our NCCs (~10 μm thick) may become significant if further increasing the indentation depth from 2 μm.

Figure 6 shows the probabilities of three indentation-induced cracking modes for as-assembled and ALD-treated NCCs: (i) no cracking [e.g., Fig. S3(b)], (ii) uncontained long cracking [e.g., Fig. S3(a)], and (iii) well-defined and well-contained (WDWC) indentation-induced cracking (e.g., Fig. S4). Figure 6 indicates that, for #ALD $<$ 65, each of the ALD-treated 254 and 289 nm NCCs behaves similar to its as-assembled counterpart, i.e., none of the 254 nm NCCs show indentation-induced cracking while many of the 289 nm NCCs show the bimodal indentation fracture behavior.

Figure 6 also interestingly shows that, for 65 $\leq$ #ALD $\leq$ 80, some indentations on 289 nm NCCs induce WDWC indentation-induced cracks, while the 254 nm NCCs still show no indentation-induced cracking. Then, for #ALD $>$ 80, some indentations on both 254 and 289 nm NCCs show WDWC cracks whose probability generally increases with increasing #ALD; in fact, all indentations on the 144ALD 254 and 289 nm NCCs show WDWC cracking.

It should be noted that, while some indentations on the as-assembled and ALD-treated 289 nm NCCs show very long uncontained indentation-induced cracks even at up to 115ALD, none of the as-assembled and ALD-treated 254 nm NCCs show this type of long cracks. Thus, according to the aforementioned mechanism of RC stress assisted cracking,[79,80] the 254 nm NCCs may be at an overall more relaxed condition with minimal RC stress compared to the 289 nm NCCs, and the calculation of K_c and the observation of fracture behavior for 254 nm NCCs would be more intrinsic with negligible influence from the RC stress.

Based on these WDWC cracks, the K_c values for 289 and 254 nm NCCs were calculated using Eq. (2) and plotted versus the ALD-thickness t normalized by particle radius [$\tau = t/(d/2)$][39] [see Fig. 5(f)]. Figure 5(f) indicates statistically good matching between the K_c values for 289 and 254 nm NCCs, probably because each domain in the 289 nm NCCs showing WDWC cracks is already in almost fully relaxed condition (similar to that for 254 nm NCCs as aforementioned). Thus, Fig. 5(f) may be considered as a master K_c curve for Al_2O_3 ALD-treated SiO_2 NCCs composed of monodisperse NCs of the two particle sizes.

Figure 5(f) shows that K_c is roughly proportional to #ALD for $0.03 < \tau < 0.08$, implying that, if K_c always monotonically increases with τ, $K_c \approx 0.156 \pm 0.071$ MPa $m^{1/2}$ at $\tau = 0.031$ would be a large overestimate for the as-assembled NCCs' K_c. Thus, Fig. 5(f) implies that, compared to the untreated NCCs, the ALD treatment at $\tau \approx 0.08$ would toughen the NCCs by much larger than 300%, which is a large toughening effect.

It should be mentioned that, it is very difficult to measure the facture toughness for NCCs after sintering because the material become too brittle for reliable measurement. For instance, 1 μm indentations did not generate crack [see Figs. 2(a) and 2(d)], whereas each 2 μm indentation caused severe cracking of an entire NCC domain or complete delamination of the NCC film [see Fig. 5(d)]. This result again indicates the limitation of sintering as a mechanical reinforcement method for NCCs due to the embrittlement effect.

IV. CONCLUSIONS

Silica NCCs were systematically treated using sintering and Al_2O_3 ALD and then characterized by nanoindentation. Both sintering and ALD treatments can locally harden and stiffen the NCCs. The IPB strength

https://doi.org/10.1557/jmr.2015.347 Published online by Cambridge University Press

increases with increasing the sintering temperature and ALD-cycle number. One major difference between the two reinforcement methods lies in the crack formation upon treatment. While sintering suffers from serious cracking issues significantly degrading the integrity of NCCs, ALD-treatment can simultaneously harden, stiffen, and toughen the NCCs without inducing any secondary cracking. By using ALD treatment, the toughness of NCCs can increase much larger than 300% compared to the as-assembled NCC. This finding highlights the versatility of ALD as a reinforcement method for nanoparticle assemblies and potentially nanoporous materials.

ACKNOWLEDGMENTS

G. Feng acknowledges financial support from an NSF Award (CBET-1235769). D. Zhang is supported by a Villanova University Research Scholarship. D. Lee acknowledges financial support from an NSF CAREER Award (DMR-1055594) and the PENN MRSEC DMR11-20901 through the NSF. We thank C. Townend for helping on designing and machining the NCC-fabrication cell. We also appreciate the technical supports from J. Hay and G. Min of Keysight Technologies Inc. (formerly Agilent Technologies Electronic Measurement Division) as well as from K. Park and W. Oliver of Nanomechanics, Inc. We also want to thank Eric Johnston of Singh Center for Nanotechnology at the University of Pennsylvania for allowing us to use a Filmetrics 40 system. Moreover, we want to appreciate the help and sample evaluation from Jim Elman of Filmetrics Inc.

REFERENCES

1. J.H. Holtz and S.A. Asher: Polymerized colloidal crystal hydrogel films as intelligent chemical sensing materials. *Nature* **389**(6653), 829 (1997).
2. Y.A. Vlasov, X-Z. Bo, J.C. Sturm, and D.J. Norris: On-chip natural assembly of silicon photonic bandgap crystals. *Nature* **414**, 289 (2001).
3. S. Sun, C.B. Murray, D. Weller, L. Folks, and A. Moser: Monodisperse FePt nanoparticles and ferromagnetic FePt nanocrystal superlattices. *Science* **287**(5460), 1989 (2000).
4. S.A. Rinne, F. Garcia-Santamaria, and P.V. Braun: Embedded cavities and waveguides in three-dimensional silicon photonic crystals. *Nat. Photonics* **2**(1), 52 (2008).
5. Y. Zhao and I. Avrutsky: Two-dimensional colloidal crystal corrugated waveguides. *Opt. Lett.* **24**(12), 817 (1999).
6. E. Istrate and E.H. Sargent: Photonic crystal heterostructures—resonant tunnelling, waveguides and filters. *J. Opt. A: Pure Appl. Opt.* **4**(6), S242 (2002).
7. K. Lee and S.A. Asher: Photonic crystal chemical sensors: pH and ionic strength. *J. Am. Chem. Soc.* **122**(39), 9534 (2000).
8. L. Zhang, J.H. Prosser, G. Feng, and D. Lee: Mechanical properties of atomic layer deposition-reinforced nanoparticle thin films. *Nanoscale* **4**(20), 6543 (2012).
9. M.I. Dafinone, G. Feng, T. Brugarolas, K.E. Tettey, and D. Lee: Mechanical reinforcement of nanoparticle thin films using atomic layer deposition. *ACS Nano* **5**(6), 5078 (2011).
10. F. Gallego-Gómez, V. Morales Flórez, Á. Blanco, N. de la Rosa Fox, and C. López: Water-dependent micromechanical and rheological properties of silica colloidal crystals studied by nanoindentation. *Nano Lett.* **12**(9), 4920 (2012).
11. J. Zhou, H. Li, L. Ye, J. Liu, J. Wang, T. Zhao, L. Jiang, and Y. Song: Facile fabrication of tough SiC inverse opal photonic crystals. *J. Phys. Chem. C* **114**(50), 22303 (2010).
12. Z. Shen, Y. Yang, F. Lu, B. Bao, and B. You: Self-assembly of binary particles and application as structural colors. *Polym. Chem.* **3**(9), 2495 (2012).
13. H. Miguez, A. Blanco, C. Lopez, F. Meseguer, H.M. Yates, M.E. Pemble, F. Lopez-Tejeira, F.J. Garcia-Vidal, and J. Sanchez-Dehesa: Face centered cubic photonic bandgap materials based on opal-semiconductor composites. *J. Lightwave Technol.* **17**(11), 1975 (1999).
14. R. Mayoral, J. Requena, J.S. Moya, C. López, A. Cintas, H. Miguez, F. Meseguer, L. Vázquez, M. Holgado, and Á. Blanco: 3D Long-range ordering in an SiO_2 submicrometer-sphere sintered superstructure. *Adv. Mater.* **9**(3), 257 (1997).
15. S.L. Kuai, Y.Z. Zhang, V.V. Truong, and X.F. Hu: Improvement of optical properties of silica colloidal crystals by sintering. *Appl. Phys. A* **74**(1), 89 (2002).
16. T. Van Le, E.E. Ross, T.R.C. Velarde, M.A. Legg, and M.J. Wirth: Sintered silica colloidal crystals with fully hydroxylated surfaces. *Langmuir* **23**(16), 8554 (2007).
17. H. Míguez, F. Meseguer, C. López, Á. Blanco, J.S. Moya, J. Requena, A. Mifsud, and V. Fornés: Control of the photonic crystal properties of fcc-packed submicrometer SiO_2 spheres by sintering. *Adv. Mater.* **10**(6), 480 (1998).
18. D. Gouvêa and R.H.R. Castro: Sintering: The role of interface energies. *Appl. Surf. Sci.* **217**(1–4), 194 (2003).
19. B. Gates, S.H. Park, and Y. Xia: Tuning the photonic bandgap properties of crystalline arrays of polystyrene beads by annealing at elevated temperatures. *Adv. Mater.* **12**(9), 653 (2000).
20. N. Machii and A.M. Nakamura: Experimental study on static and impact strength of sintered agglomerates. *Icarus* **211**, 885 (2011).
21. A.A. Zakhidov, R.H. Baughman, Z. Iqbal, C. Cui, I. Khayrullin, S.O. Dantas, J. Marti, and V.G. Ralchenko: Carbon structures with three-dimensional periodicity at optical wavelengths. *Science* **282** (5390), 897 (1998).
22. L. Pallavidino, D.S. Razo, F. Geobaldo, A. Balestreri, D. Bajoni, M. Galli, L.C. Andreani, C. Ricciardi, E. Celasco, M. Quaglio, and F. Giorgis: Synthesis, characterization and modelling of silicon based opals. *J. Non-Cryst. Solids* **352**(9–20), 1425 (2006).
23. S-L. Kuai, V-V. Truong, A. Haché, and X-F. Hu: A comparative study of inverted-opal titania photonic crystals made from polymer and silica colloidal crystal templates. *J. Appl. Phys.* **96**(11), 5982 (2004).
24. S. Kuai, S. Badilescu, G. Bader, R. Brüning, X. Hu, and V.V. Truong: Preparation of large-area 3D ordered macroporous titania films by silica colloidal crystal templating. *Adv. Mater.* **15**(1), 73 (2003).
25. B. Hatton, L. Mishchenko, S. Davis, K.H. Sandhage, and J. Aizenberg: Assembly of large-area, highly ordered, crack-free inverse opal films. *Proc. Natl. Acad. Sci. U. S. A.* **107**(23), 10354 (2010).
26. N.P. Johnson, D.W. McComb, A. Richel, B.M. Treble, and R.M. De La Rue: Synthesis and optical properties of opal and inverse opal photonic crystals. *Synth. Met.* **116**(1–3), 469 (2001).
27. X. Chen, L. Wang, Y. Wen, Y. Zhang, J. Wang, Y. Song, L. Jiang, and D. Zhu: Fabrication of closed-cell polyimide inverse opal photonic crystals with excellent mechanical properties and thermal stability. *J. Mater. Chem.* **18**(19), 2262 (2008).
28. Z.Z. Gu, S. Kubo, A. Fujishima, and O. Sato: Infiltration of colloidal crystal with nanoparticles using capillary forces: A simple technique for the fabrication of films with an ordered porous structure. *Appl. Phys. A* **74**, 127 (2002).

https://doi.org/10.1557/jmr.2015.347 Published online by Cambridge University Press

29. S. Kubo, Z-Z. Gu, K. Takahashi, A. Fujishima, H. Segawa, and O. Sato: Tunable photonic band gap crystals based on a liquid crystal-infiltrated inverse opal structure. *J. Am. Chem. Soc.* **126**(26), 8314 (2004).
30. J.S. King, D.P. Gaillot, E. Graugnard, and C.J. Summers: Conformally back-filled, non-close-packed inverse-opal photonic crystals. *Adv. Mater.* **18**(8), 1063 (2006).
31. E. Graugnard, J.S. King, D.P. Gaillot, and C.J. Summers: Sacrificial-layer atomic layer deposition for fabrication of non-close-packed inverse-opal photonic crystals. *Adv. Funct. Mater.* **16**(9), 1187 (2006).
32. A. Blanco, E. Chomski, S. Grabtchak, M. Ibisate, S. John, S.W. Leonard, C. Lopez, F. Meseguer, H. Miguez, J.P. Mondia, G.A. Ozin, O. Toader, and H.M. van Driel: Large-scale synthesis of a silicon photonic crystal with a complete three-dimensional bandgap near 1.5 micrometres. *Nature* **405**(6785), 437 (2000).
33. T. Poppe: Sintering of highly porous silica-particle samples: Analogues of early Solar-system aggregates. *Icarus* **164**(1), 139 (2003).
34. H. Masuda, K. Higashitani, and H. Yoshida: *Powder Technology Handbook* (CRC Press, Boca Raton, 2006).
35. R.H.R. Castro and K.v. Benthem: *Sintering Mechanisms of Convention Nanodensification and Field Assisted Processes* (Springer, Verlag Berlin Heidelberg, 2013).
36. R.M. German: *Sintering: From Empirical Observations to Scientific Principles* (Elsevier, Oxford, 2014).
37. Z.Z. Fang: *Sintering of Advanced Materials Fundamentals and Processes* (Woodhead Publishing, Philadelphia, 2010).
38. D. Zhang, L. Zhang, D. Lee, X. Cheng, and G. Feng: Suppressing unstable deformation of nanocolloidal crystals with atomic layer deposition. *Mater. Sci. Eng., A* **639**, 514 (2015).
39. D. Zhang, L. Zhang, D. Lee, X. Cheng, and G. Feng: Reinforcing nanocolloidal crystals by tuning interparticle bonding via atomic layer deposition. *Acta Mater.* **95**, 216 (2015).
40. F. Gallego-Gomez, A. Blanco, and C. Lopez: Exploration and exploitation of water in colloidal crystals. *Adv. Mater.* **27**(17), 2686 (2015).
41. H. Miguez, N. Tetreault, B. Hatton, S.M. Yang, D. Perovic, and G. A. Ozin: Mechanical stability enhancement by pore size and connectivity control in colloidal crystals by layer-by-layer growth of oxide. *Chem. Commun.* (22), 2736 (2002).
42. H. Li, J. Wang, Z. Pan, L. Cui, L. Xu, R. Wang, Y. Song, and L. Jiang: Amplifying fluorescence sensing based on inverse opal photonic crystal toward trace TNT detection. *J. Mater. Chem.* **21**(6), 1730 (2011).
43. J. Wang, Y. Wen, H. Ge, Z. Sun, Y. Zheng, Y. Song, and L. Jiang: Simple fabrication of full color colloidal crystal films with tough mechanical strength. *Macromol. Chem. Phys.* **207**(6), 596 (2006).
44. H. Míguez, S.M. Yang, N. Tétreault, and G.A. Ozin: Oriented free-standing three-dimensional silicon inverted colloidal photonic crystal microfibers. *Adv. Mater.* **14**(24), 1805 (2002).
45. J.F. Galisteo, F. García-Santamaría, D. Golmayo, B.H. Juárez, C. López, and E. Palacios: Self-assembly approach to optical metamaterials. *J. Opt. A: Pure Appl. Opt.* **7**(2), S244 (2005).
46. Z.A. Sechrist, B.T. Schwartz, J.H. Lee, J.A. McCormick, R. Piestun, W. Park, and S.M. George: Modification of opal photonic crystals using Al_2O_3 atomic layer deposition. *Chem. Mater.* **18**(15), 3562 (2006).
47. J.H. Moon and S. Yang: Chemical aspects of three-dimensional photonic crystals. *Chem. Rev.* **110**(1), 547 (2009).
48. S.M. George: Atomic layer deposition: An overview. *Chem. Rev.* **110**, 111 (2010).
49. M. Leskel and M. Ritala: Atomic layer deposition chemistry: Recent developments and future challenges. *Angew. Chem., Int. Ed.* **42**, 5548 (2003).
50. H. Kim, H.B.R. Lee, and W.J. Maeng: Applications of atomic layer deposition to nanofabrication and emerging nanodevices. *Thin Solid Films* **517**(8), 2563 (2009).
51. M. Leskelä and M. Ritala: Atomic layer deposition (ALD): From precursors to thin film structures. *Thin Solid Films* **409**(1), 138 (2002).
52. M. Scharrer, X. Wu, A. Yamilov, H. Cao, and R.P.H. Chang: Fabrication of inverted opal ZnO photonic crystals by atomic layer deposition. *Appl. Phys. Lett.* **86**(15), 151113 (2005).
53. A. Blanco, F. Gallego-Gómez, and C. López: Nanoscale morphology of water in silica colloidal crystals. *J. Phys. Chem. Lett.* **4**(7), 1136 (2013).
54. F. Gallego-Gómez, A. Blanco, V. Canalejas-Tejero, and C. López: Water-dependent photonic bandgap in silica artificial opals. *Small* **7**(13), 1838 (2011).
55. W. Stöber, A. Fink, and E. Bohn: Controlled growth of monodisperse silica spheres in the micron size range. *J. Colloid Interface Sci.* **26**(1), 62 (1968).
56. L. Wang, Y. Wan, Y. Li, Z. Cai, H-L. Li, X.S. Zhao, and Q. Li: Binary colloidal crystals fabricated with a horizontal deposition method. *Langmuir* **25**(12), 6753 (2009).
57. Q. Yan, X.S. Zhao, and Z. Zhou: Fabrication of colloidal crystal heterostructures using a horizontal deposition method. *J. Cryst. Growth* **288**(1), 205 (2006).
58. Q. Yan, Z. Zhou, and X.S. Zhao: Inward-growing self-assembly of colloidal crystal films on horizontal substrates. *Langmuir* **21**(7), 3158 (2005).
59. W.C. Olive and G.M. Pharr: An Improved technique for determining hardness and elastic modulus using load and displacement sensing indentation experiments. *J. Mater. Res.* **7**, 1564 (1992).
60. J. Hay and B. Crawford: Measuring substrate-independent modulus of thin films. *J. Mater. Res.* **26**(06), 727 (2011).
61. S.M. Han, R. Saha, and W.D. Nix: Determining hardness of thin films in elastically mismatched film-on-substrate systems using nanoindentation. *Acta Mater.* **54**, 1571 (2006).
62. D. Lorenz, A. Zeckzer, U. Hilpert, P. Grau, H. Johansen, and H.S. Leipner: Pop-in effect as homogeneous nucleation of dislocations during nanoindentation. *Phys. Rev. B* **67**(17), 172101 (2003).
63. F. Gallego-Gómez, A. Blanco, and C. López: In Situ optical study of water sorption in silica colloidal crystals. *J. Phys. Chem. C* **116**(34), 18222 (2012).
64. A. Chiappini, C. Armellini, A. Chiasera, M. Ferrari, Y. Jestin, M. Mattarelli, M. Montagna, E. Moser, G. Nunzi Conti, S. Pelli, G.C. Righini, M. Clara Gonçalves, and R.M. Almeida: Design of photonic structures by sol–gel-derived silica nanospheres. *J. Non-Cryst. Solids* **353**(5–7), 674 (2007).
65. F. Garcia-Santamaria, H. Miguez, M. Ibisate, F. Meseguer, and C. Lopez: Refractive index properties of calcined silica submicrometer spheres. *Langmuir* **18**, 1942 (2002).
66. D. Chrobak, K. Nordlund, and R. Nowak: Nondislocation origin of GaAs nanoindentation pop-in event. *Phys. Rev. Lett.* **98**(4), 045502 (2007).
67. W.J. Wright, R. Saha, and W.D. Nix: Deformation mechanisms of the $Zr_{40}Ti_{14}Ni_{10}Cu_{12}Be_{24}$ bulk metallic glass. *Mater. Trans.* **42**(4), 642 (2001).
68. M.S. Tirumkudulu and W.B. Russel: Cracking in drying latex films. *Langmuir* **21**(11), 4938 (2005).
69. E.R. Dufresne, E.I. Corwin, N.A. Greenblatt, J. Ashmore, D.Y. Wang, A.D. Dinsmore, J.X. Cheng, X.S. Xie, J.W. Hutchinson, and D.A. Weitz: Flow and fracture in drying nanoparticle suspensions. *Phys. Rev. Lett.* **91**(22), 224501 (2003).
70. K.B. Singh and M.S. Tirumkudulu: Cracking in drying colloidal films. *Phys. Rev. Lett.* **98**(21), 218302 (2007).

https://doi.org/10.1557/jmr.2015.347 Published online by Cambridge University Press

71. A. Jagota and C.Y. Hui: Mechanics of sintering thin films—II. Cracking due to self-stress. *Mech. Mater.* **11**(3), 221 (1991).
72. L. Grabner: Spectroscopic technique for the measurement of residual stress in sintered Al_2O_3. *J. Appl. Phys.* **49**(2), 580 (1978).
73. B.R. Lawn, A.G. Evans, and D.B. Marshall: Elastic/plastic indentation damage in ceramics: The median/radial crack system. *J. Am. Ceram. Soc.* **63**(9–10), 574 (1980).
74. J.H. Lee, Y.F. Gao, K.E. Johanns, and G.M. Pharr: Cohesive interface simulations of indentation cracking as a fracture toughness measurement method for brittle materials. *Acta Mater.* **60**(15), 5448 (2012).
75. A.A. Volinsky, J.B. Vella, and W.W. Gerberich: Fracture toughness, adhesion and mechanical properties of low-K dielectric thin films measured by nanoindentation. *Thin Solid Films* **429**(1–2), 201 (2003).
76. G.M. Pharr: Measurement of mechanical properties by ultra-low load indentation. *Mater. Sci. Eng., A* **253**(1–2), 151 (1998).
77. T. Scholz, G.A. Schneider, J. Muñoz-Saldaña, and M.V. Swain: Fracture toughness from submicron derived indentation cracks. *Appl. Phys. Lett.* **84**(16), 3055 (2004).
78. D.S. Hardinga, W.C. Olivera, and G.M. Pharra: Cracking during nanoindentation and its use in the measurement of fracture toughness. *Mater. Res. Soc. Symp. Proc.* **356**, 663 (1995).
79. C. Anunmana, K.J. Anusavice, and J.J. Mecholsky: Residual stress in glass: Indentation crack and fractography approaches. *Dent. Mater.* **25**(11), 1453 (2009).
80. K. Zeng and D. Rowcliffe: Experimental measurement of residual stress field around sharp indentation in glass. *J. Am. Ceram. Soc.* **77**(2), 524 (1994).

Supplementary Material

To view supplementary material for this article, please visit http://dx.doi.org/jmr.2015.347.

https://doi.org/10.1557/jmr.2015.347 Published online by Cambridge University Press